Numerical renormalization group for impurity quantum phase transitions: structure of critical fixed points

2005 J. Phys.: Condens. Matter 17 6935

(http://iopscience.iop.org/0953-8984/17/43/012)

INSTITUTE OF PHYSICS PUBLISHING JOURNAL OF PHYSICS: CONDENSED MATTER

J. Phys.: Condens. Matter **17** (2005) 6935–6957 doi:10.1088/0953-8984/17/43/012

Numerical renormalization group for impurity quantum phase transitions: structure of critical fixed points

Hyun-Jung Lee[1], **Ralf Bulla**[1] **and Matthias Vojta**[2]

[1] Theoretische Physik III, Elektronische Korrelationen und Magnetismus, Institut für Physik, Universität Augsburg, D-86135 Augsburg, Germany
[2] Institut für Theorie der Kondensierten Materie, Universität Karlsruhe, D-76128 Karlsruhe, Germany

Received 4 July 2005
Published 14 October 2005
Online at stacks.iop.org/JPhysCM/17/6935

Abstract

The numerical renormalization group method is used to investigate zero-temperature phase transitions in quantum impurity systems, in particular in the particle–hole symmetric soft-gap Anderson model. The model displays two stable phases whose fixed points can be built up of non-interacting single-particle states. In contrast, the quantum phase transitions turn out to be described by interacting fixed points, and their excitations cannot be described in terms of free particles. We show that the structure of the many-body spectrum of these critical fixed points can be understood using renormalized perturbation theory close to certain values of the bath exponents which play the role of critical dimensions. Contact is made with perturbative renormalization group calculations for the soft-gap Anderson and Kondo models. A complete description of the quantum critical many-particle spectra is achieved using suitable marginal operators; technically this can be understood as epsilon-expansion for full many-body spectra.

(Some figures in this article are in colour only in the electronic version)

1. Introduction

Zero-temperature phase transitions in quantum impurity models have recently attracted considerable interest (for reviews see [1–3]). These transitions can be observed in systems where a zero-dimensional boundary with internal degrees of freedom (the impurity) interacts with an extended bath of fermions or bosons. Examples of impurity models with non-trivial phase transitions include extensions of the Kondo model where one or two magnetic impurities couple to fermionic baths [1], the spin-boson model describing a two-level system coupling to a dissipative environment [4, 5], as well as so-called Bose–Fermi Kondo models for localized spins interacting with both fermionic and bosonic baths. Impurity phase transitions are of

relevance for impurities in correlated bulk systems (e.g. superconductors [6]), for multilevel impurities like fullerene molecules [7], as well as for nanodevices like coupled quantum dots [8] or point contacts under the influence of dissipative noise [9, 10]. In addition, impurity phase transitions have been argued to describe aspects of so-called local quantum criticality in correlated lattice systems. Here, the framework of dynamical mean-field theory is employed to map, for example, the Kondo lattice model onto a single-impurity Bose–Fermi Kondo model supplemented by self-consistency conditions; for details, see [11].

Diverse techniques have been used to investigate impurity phase transitions, ranging from static and dynamic large-N calculations [12], conformal field theory [3], perturbative renormalization group (RG) [1, 6, 13] and the local-moment approach [14, 15] to various numerical methods. In particular, significant progress has been made using the numerical renormalization group (NRG) technique, originally developed by Wilson for the Kondo problem [16]. The NRG combines numerically exact diagonalization with the idea of the renormalization group, where progressively smaller energy scales are treated in the course of the calculation. NRG calculations are non-perturbative and are able to access arbitrarily small energies and temperatures. Apart from static and dynamic observables, the NRG provides information about the many-body excitation spectrum of the system at every stage of the RG flow. Thus, it allows us to identify fixed points through their fingerprints in the level structure. A detailed understanding of the NRG levels is usually possible if the fixed point can be described by non-interacting bosons or fermions—this is the case for most stable fixed points of impurity models, for example, the strong-coupling (screened) fixed point of a standard Kondo model. Intermediate-coupling fixed points, usually being interacting, have a completely different NRG level structure, i.e., smaller degeneracies and non-equidistant levels. They cannot be cast into a free-particle description, with the remarkable exception of the two-channel Kondo fixed point which is known to have a representation in terms of free Majorana fermions [17]. In general, the NRG fixed-point spectrum at impurity transitions is fully universal, apart from a non-universal overall prefactor and discretization effects.

The purpose of this paper is to demonstrate that a complete understanding of the NRG many-body spectrum of critical fixed points is actually possible, by utilizing renormalized perturbation theory around a non-interacting fixed point. In the soft-gap Anderson model, this approach can be employed near certain values of the bath exponent which can be identified as critical dimensions. Using the knowledge from perturbative RG calculations, which yield the relevant coupling constants being parametrically small near the critical dimension, we can construct the entire quantum critical many-body spectrum from a free-fermion model supplemented by a small perturbation. In other words, we shall perform epsilon-expansions to determine a complete many-body spectrum (instead of certain renormalized couplings or observables). Conversely, our method allows us to identify relevant degrees of freedom and their marginal couplings by carefully analysing the NRG spectra near critical dimensions of impurity quantum phase transitions.

The paper is organized as follows. In section 2 we give a brief introduction to the physics of the soft-gap Anderson model and its quantum phase transitions. Section 3 summarizes the recent results from perturbative RG for both the soft-gap Anderson and Kondo models. Section 4 describes the NRG approach which is used here to obtain information about the structure of the quantum critical points. The main part of the paper is section 5, in which we discuss (i) the numerical data for the structure of the quantum critical points and (ii) the analytical description of these interacting fixed points close to the upper (lower) critical dimension $r = 0$ ($r = 1/2$). The main conclusions of the paper are summarized in section 6, where we also mention other problems for which an analysis of the type presented here might be useful.

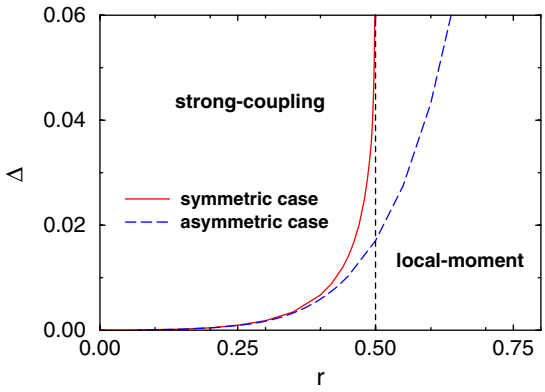

Figure 1. $T = 0$ phase diagram for the soft-gap Anderson model in the p–h symmetric case (solid line, $U = 10^{-3}$, $\varepsilon_f = -0.5 \times 10^{-3}$, conduction band cutoff at -1 and 1) and the p–h asymmetric case (dashed line, $\varepsilon_f = -0.4 \times 10^{-3}$); Δ measures the hybridization strength, $\widetilde{\Delta}(\omega) = \Delta|\omega|^r$.

2. Soft-gap Anderson model

The Hamiltonian of the soft-gap Anderson model [12] is given by

$$H = \varepsilon_f \sum_\sigma f_\sigma^\dagger f_\sigma + U f_\uparrow^\dagger f_\uparrow f_\downarrow^\dagger f_\downarrow + \sum_{k\sigma} \varepsilon_k c_{k\sigma}^\dagger c_{k\sigma} + V \sum_{k\sigma} \left(f_\sigma^\dagger c_{k\sigma} + c_{k\sigma}^\dagger f_\sigma \right). \tag{1}$$

This model describes the coupling of electronic degrees of freedom at an impurity site (operators $f_\sigma^{(\dagger)}$) to a fermionic bath (operators $c_{k\sigma}^{(\dagger)}$) via a hybridization V. The f-electrons are subject to a local Coulomb repulsion U, while the fermionic bath consists of a non-interacting conduction band with dispersion ε_k. The model equation (1) has the same form as the single-impurity Anderson model [18] but for the soft-gap model we require that the hybridization function $\widetilde{\Delta}(\omega) = \pi V^2 \sum_k \delta(\omega - \varepsilon_k)$ has a soft-gap at the Fermi level, $\widetilde{\Delta}(\omega) = \Delta|\omega|^r$, with an exponent $r > 0$. This translates into a local conduction band density of states $\rho(\omega) = \rho_0|\omega|^r$ at low energies. In the numerical calculations we used a band where this power law extends over the whole bandwidth D, i.e., from $\omega = -D/2$ to $+D/2$, and we have $\rho_0 = (2/D)^{r+1}(r+1)/2$. However, the universal low-temperature physics to be discussed in the following does not depend on the details of the density of states at high energies, and consequently we will use the low-energy prefactor of the density of states, ρ_0, to represent the dimensionful energy scale of the problem. Assuming a particle–hole symmetric band, the model (1) is particle–hole symmetric for $\epsilon_f = -U/2$.

The soft-gap Anderson model (1) with $0 < r < \infty$ displays a very rich behaviour, in particular a continuous transition between a local-moment (LM) and a strong-coupling (SC) phase. Figure 1 shows a typical phase diagram for the soft-gap Anderson model. In the particle–hole (p–h) symmetric case (solid line) the critical coupling Δ_c diverges at $r = \frac{1}{2}$, and no screening occurs for $r > \frac{1}{2}$ [19, 20]. No divergence occurs for p–h asymmetry (dashed line) [19].

We now briefly describe the properties of the fixed points in the soft-gap Anderson and Kondo models [19]. Due to the power-law conduction band density of states, already the stable LM and SC fixed points show non-trivial behaviour [19, 20]. The LM phase has the properties of a free spin $\frac{1}{2}$ with residual entropy $S_{\rm imp} = k_{\rm B} \ln 2$ and low-temperature impurity susceptibility $\chi_{\rm imp} = 1/(4k_{\rm B}T)$, but the leading corrections show r-dependent power laws. The p–h symmetric SC fixed point has very unusual properties, namely $S_{\rm imp} = 2rk_{\rm B} \ln 2$,

$\chi_{\rm imp} = r/(8k_{\rm B}T)$ for $0 < r < \frac{1}{2}$. In contrast, the p–h asymmetric SC fixed point simply displays a completely screened moment, $S_{\rm imp} = T\chi_{\rm imp} = 0$. The impurity spectral function follows an ω^r power law at both the LM and the asymmetric SC fixed point, whereas it diverges as ω^{-r} at the symmetric SC fixed point—this 'peak' can be viewed as a generalization of the Kondo resonance in the standard case ($r = 0$), and scaling of this peak is observed upon approaching the SC–LM phase boundary [14, 20]. At the critical point, non-trivial behaviour corresponding to a fractional moment can be observed: $S_{\rm imp} = k_{\rm B}\mathcal{C}_S(r)$, $\chi_{\rm imp} = \mathcal{C}_\chi(r)/(k_{\rm B}T)$ with $\mathcal{C}_S, \mathcal{C}_\chi$ being universal functions of r (see [19, 21]). The spectral functions at the quantum critical points display an ω^{-r} power law (for $r < 1$) with a remarkable 'pinning' of the critical exponent.

3. Results from perturbative RG

The Anderson model (1) is equivalent to a Kondo model when charge fluctuations on the impurity site are negligible. The Hamiltonian for the soft-gap Kondo model can be written as

$$H = J\vec{S}\cdot\vec{s}_0 + \sum_{k\sigma}\varepsilon_k c^\dagger_{k\sigma}c_{k\sigma} \tag{2}$$

where $\vec{s}(0) = \sum_{kk'\sigma\sigma'} c^\dagger_{k\sigma}\vec{\sigma}_{\sigma\sigma'}c_{k'\sigma'}/2$ is the conduction electron spin at the impurity site $\mathbf{r}=0$, and the conduction electron density of states follows a power law $\rho(\omega) = \rho_0|\omega|^r$ as above.

3.1. RG near $r = 0$

For small values of the density of states exponent r, the phase transition in the pseudogap Kondo model can be accessed from the weak-coupling limit, using a generalization of Anderson's poor man's scaling. Power counting about the local-moment fixed point (LM) shows that $\dim[J] = -r$, i.e., the Kondo coupling is marginal for $r = 0$. We introduce a renormalized dimensionless Kondo coupling j according to

$$\rho_0 J = \mu^{-r} j \tag{3}$$

where μ plays the role of a UV cutoff. The flow of the renormalized Kondo coupling j is given by the beta function

$$\beta(j) = rj - j^2 + \mathcal{O}(j^3). \tag{4}$$

For $r > 0$ there is a stable fixed point at $j^* = 0$ corresponding to the local-moment phase (LM). An unstable fixed point, controlling the transition to the strong-coupling phase, exists at

$$j^* = r, \tag{5}$$

and the critical properties can be determined in a double expansion in r and j [6]. The p–h asymmetry is irrelevant, i.e., a potential scattering term E scales to zero according to $\beta(e) = re$ (where $\rho_0 E = \mu^{-r}e$), thus the above expansion captures the p–h symmetric critical fixed point (SCR). As the dynamical exponent ν, $1/\nu = r + \mathcal{O}(r^2)$, diverges as $r \to 0^+$, $r = 0$ plays the role of a lower-critical dimension of the transition under consideration.

3.2. RG near $r = 1/2$

For r near $1/2$ the p–h symmetric critical fixed point moves to strong Kondo coupling, and the language of the p–h symmetric Anderson model becomes more appropriate [13]. First, the conduction electrons can be integrated out exactly, yielding a self-energy $\Sigma_f = V^2 G_{c0}$ for

the f electrons, where G_{c0} is the bare conduction electron Green's function at the impurity location. In the low-energy limit the f electron propagator is then given by

$$G_f(\mathrm{i}\omega_n)^{-1} = \mathrm{i}\omega_n - \mathrm{i}A_0\,\mathrm{sgn}(\omega_n)\,|\omega_n|^r \tag{6}$$

where the $|\omega_n|^r$ self-energy term dominates for $r < 1$, and the prefactor A_0 is

$$A_0 = \frac{\pi\rho_0 V^2}{\cos\frac{\pi r}{2}}. \tag{7}$$

Equation (6) describes the physics of a non-interacting resonant level model with a soft-gap density of states. Interestingly, the impurity spin is not fully screened for $r > 0$, and the residual entropy is $2r \ln 2$. This precisely corresponds to the symmetric strong-coupling (SC) phase of the soft-gap Anderson and Kondo models [19].

Dimensional analysis, using $\dim[f] = (1-r)/2$ (where f represents the dressed fermion according to equation (6)), now shows that the interaction term U of the Anderson model scales as $\dim[U] = 2r - 1$, i.e., it is marginal at $r = 1/2$. This suggests a perturbative expansion in U around the SC fixed point. We introduce a dimensionless renormalized on-site interaction u via

$$U = \mu^{2r-1} A_0^2 u. \tag{8}$$

The beta function receives the lowest non-trivial contribution at two-loop order and reads [13]

$$\beta(u) = (1-2r)\,u - \frac{3(\pi - 2\ln 4)}{\pi^2}\,u^3 + \mathcal{O}(u^5). \tag{9}$$

For $r < 1/2$ a non-interacting stable fixed point is at $u^* = 0$—this is the symmetric strong-coupling fixed point; it becomes unstable for $r > 1/2$. Additionally, for $r < 1/2$ there is a pair of critical fixed points (SCR, SCR′) located at $u^{*2} = \pi^2(1-2r)/[3(\pi - 2\ln 4)]$, i.e.,

$$u^* = \pm 4.22\sqrt{1/2 - r}. \tag{10}$$

These fixed points describe the transition between an unscreened (spin or charge) moment phase and the symmetric strong-coupling phase [13].

Summarizing, both (4) and (9) capture the same critical SCR fixed point. This fixed point can be accessed either by an expansion around the weak-coupling LM fixed point, i.e., around the decoupled impurity limit, valid for $r \ll 1$, or by an expansion around the strong-coupling SC fixed point, i.e., around a non-interacting resonant-level (or Anderson) impurity, and this expansion is valid for $1/2 - r \ll 1$.

4. Numerical renormalization group

Here we describe the numerical renormalization group method, suitably extended to handle non-constant couplings $\widetilde{\Delta}(\omega)$ (see [19, 20, 22]). This method allows a non-perturbative calculation of the many-particle spectrum and physical properties in the whole parameter regime of the model equation (1), in particular in the low-temperature limit, so that the structure of the quantum critical points is accessible, as discussed in section 5.

A detailed discussion of how the NRG can be applied to the soft-gap Anderson model can be found in [19, 20, 22]. Here we focus on those aspects of the approach necessary to understand how information on the fixed points can be extracted.

The NRG is based on a logarithmic discretization of the energy axis, i.e. one introduces a parameter Λ and divides the energy axis into intervals $[-\Lambda^{-n}, -\Lambda^{-(n+1)}]$ and $[\Lambda^{-(n+1)}, \Lambda^{-n}]$

for $n = 0, 1, \ldots, \infty$ (see [16, 23]). With some further manipulations the original model can be mapped onto a semi-infinite chain with the Hamiltonian

$$H = \varepsilon_f \sum_\sigma f_\sigma^\dagger f_\sigma + U f_\uparrow^\dagger f_\uparrow f_\downarrow^\dagger f_\downarrow + \sqrt{\frac{\xi_0}{\pi}} \sum_\sigma \left[f_\sigma^\dagger c_{0\sigma} + c_{0\sigma}^\dagger f_\sigma \right] + \sum_{\sigma n=0}^{\infty} \left[\varepsilon_n c_{n\sigma}^\dagger c_{n\sigma} + t_n \left(c_{n\sigma}^\dagger c_{n+1\sigma} + c_{n+1\sigma}^\dagger c_{n\sigma} \right) \right], \tag{11}$$

with

$$\xi_0 = \int_{-1}^{1} \mathrm{d}\omega \, \widetilde{\Delta}(\omega). \tag{12}$$

For a p–h symmetric conduction band, all the on-site energies ε_n vanish. If, in addition, the power law in $\widetilde{\Delta}(\omega)$ extends up to a hard cut-off ω_c (we set $\omega_c = 1$), an exact expression for the hopping matrix elements t_n can be given [20]:

$$t_n = \Lambda^{-n/2} \frac{r+1}{r+2} \frac{1-\Lambda^{-(r+2)}}{1-\Lambda^{-(r+1)}} \left[1-\Lambda^{-(n+r+1)}\right] \times \left[1-\Lambda^{-(2n+r+1)}\right]^{-1/2} \left[1-\Lambda^{-(2n+r+3)}\right]^{-1/2} \tag{13}$$

for even n and

$$t_n = \Lambda^{-(n+r)/2} \frac{r+1}{r+2} \frac{1-\Lambda^{-(r+2)}}{1-\Lambda^{-(r+1)}} \left[1-\Lambda^{-(n+1)}\right] \times \left[1-\Lambda^{-(2n+r+1)}\right]^{-1/2} \left[1-\Lambda^{-(2n+r+3)}\right]^{-1/2} \tag{14}$$

for odd n. The semi-infinite chain is solved iteratively by starting from the impurity and successively adding chain sites. As the coupling t_n between two adjacent sites n and $n+1$ decreases as $\Lambda^{-n/2}$ for large n, the low-energy states of the chain with $n+1$ sites are generally determined by a comparatively small number N_s of states close to the ground state of the n-site system. In practice one retains only these N_s states from the n-site chain to set up the Hilbert space for the $n+1$-site chain, thus preventing the usual exponential growth of the Hilbert space as n increases. Eventually, after n_{NRG} sites have been included in the calculation, the addition of another site will not significantly change the spectrum of many-particle excitations; the spectrum is very close to that of the fixed point, and the calculation may be terminated.

In this way, the NRG iteration gives the many-particle energies E_N for a sequence of Hamiltonians H_N which correspond to the Hamiltonian equation (11) by the replacement

$$\sum_{\sigma n=0}^{\infty} \longrightarrow \sum_{\sigma n=0}^{N-1}. \tag{15}$$

An example for the dependence of the lowest-lying energy levels on the chain length (the flow diagram) is given in figure 2(c) for the soft-gap Anderson model with $r = 0.4$, $D = 2$, $U/D = 10^{-3}$ and $\Delta = 0.0075$; the parameters used for the NRG calculations are $\Lambda = 2$ and $N_s = 300$. The states are labelled by the quantum numbers Q (which characterizes the number of particles measured relative to half-filling), and the total spin, S (solid lines in figure 2 are for $(Q, S) = (1, 0)$, dashed lines for $(Q, S) = (0, 1/2)$). As mentioned above, the energy scale is reduced in each step by a factor $\Lambda^{1/2}$. To allow for a direct comparison of the energies for different chain lengths, it is thus convenient to plot $\Lambda^{N/2} E_N$ instead of the eigenvalues E_N of the N-site chain directly. Note that here and in the following we use the convention that the energies shown in the flow diagrams are proportional to the bandwidth D.

As is apparent from figure 2(c), the properties of the system in this case do not change further for chain lengths $n_{NRG} > 120$. Without going into details now, one can show that the

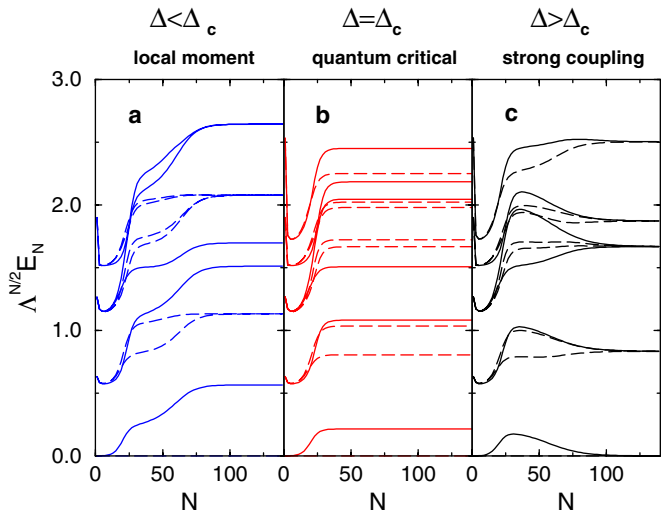

Figure 2. Flow diagrams for the low-energy many-body excitations obtained from the numerical renormalization group for the three different fixed points of the p–h symmetric soft-gap Anderson model (exponent $r = 0.4$). N is the number of iterations of the NRG procedure, Λ the NRG discretization parameter. Solid lines: $(Q, S) = (1, 0)$, dashed lines: $(Q, S) = (0, 1/2)$.

distribution of energy levels for $N > 120$ in figure 2(c) is characteristic of the SC phase of the model (see section 5).

If by contrast we choose instead a value of $\Delta = 0.006$, we obtain the flow diagram shown in figure 2(a). Here it is evident that the fixed-point level structure is entirely different from the SC solution, and indeed this particular pattern is now characteristic of the LM phase of the model. We can thus conclude, simply from inspection of the two flow diagrams, that the critical Δ_c, separating the SC and LM phases of the soft-gap Anderson model for the model parameters specified, lies in the interval [0.006, 0.0075].

Tuning the value of Δ to the critical value, Δ_c, results in the flow diagram of figure 2(b). Apparently, the structure of the fixed point at Δ_c coincides neither with the SC nor with the LM fixed point. It is clear that it cannot be simply constructed from single-particle states as for the SC and LM fixed points. An important observation is that certain degeneracies present in the SC or LM fixed points are lifted at the QCP. As shown in the following section, a further hint on the structure of the QCPs is given by the dependence of their many-particle spectra on the bath exponent r.

5. Structure of the quantum critical points

In figure 3, the many-particle spectra of the three fixed points (SC: dot–dashed lines, LM: dashed lines, and QCP: solid lines) of the symmetric soft-gap model are plotted as functions of the exponent r (for a similar figure, see figure 13 in [19]). The data are shown for an odd number of sites only and we select the lowest-lying energy levels for the subspace $Q = 1$ and $S = 0$.

As usual, the fixed-point structure of the strong coupling and local moment phases can be easily constructed from the single-particle states of a free conduction electron chain. This is discussed in more detail later. Let us now turn to the line of quantum critical points. What information can be extracted from figure 3 to understand the structure of these fixed points?

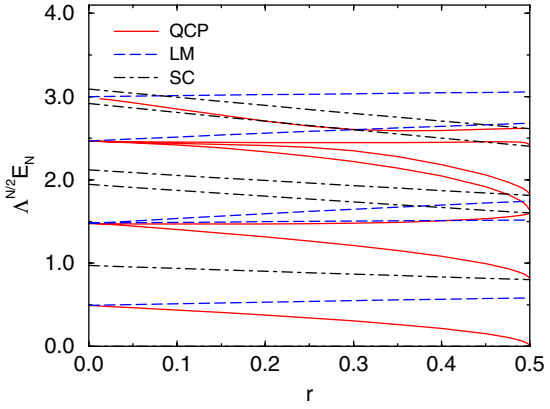

Figure 3. Dependence of the many-particle spectra for the three fixed points of the p–h symmetric soft-gap Anderson model on the exponent r: SC (dot–dashed lines), LM (dashed lines), and the (symmetric) quantum critical point (solid lines). The data are shown for the subspace $Q = 1$ and $S = 0$ only.

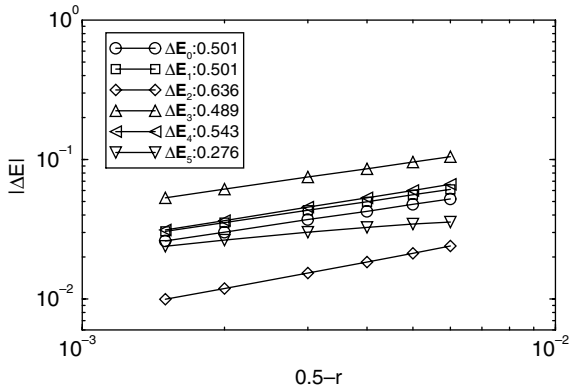

Figure 4. Difference ΔE between the energy levels of QCP and SC fixed points close to $r = 1/2$ in a double-logarithmic plot. The inset shows the values of the exponents obtained from a fit to the data points.

First we observe that the levels of the quantum critical points, $E_{N,\mathrm{QCP}}(r)$, approach the levels of the LM (SC) fixed points in the limit $r \to 0$ ($r \to 1/2$):

$$\begin{aligned} \lim_{r\to 0} \left\{E_{N,\mathrm{QCP}}(r)\right\} &= \left\{E_{N,\mathrm{LM}}(r=0)\right\}, \\ \lim_{r\to 1/2} \left\{E_{N,\mathrm{QCP}}(r)\right\} &= \left\{E_{N,\mathrm{SC}}(r=1/2)\right\}, \end{aligned} \tag{16}$$

where $\{\cdots\}$ denotes the whole set of many-particle states.

For $r \to 0$, each individual many-particle level $E_{N,\mathrm{QCP}}(r)$ deviates linearly from the levels of the LM fixed point, while the deviation from the SC levels is proportional to $\sqrt{1/2 - r}$ for $r \to 1/2$. This is illustrated in figure 4 where we plot a selection of energy differences ΔE between levels of QCP and SC fixed points close to $r = 1/2$. The inset shows the values of the exponents obtained from a fit to the data points. For some levels, there are significant deviations from the exponent $1/2$. This is because the correct exponent is only obtained in the limit $r \to 1/2$ (the QCP levels have been obtained only up to $r = 0.4985$).

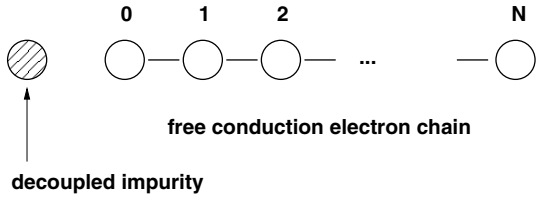

Figure 5. The spectrum of the LM fixed point is described by the impurity decoupled from the free conduction electron chain.

Note that the behaviour of the many-particle levels close to $r = 1/2$ has direct consequences for physical properties at the QCP; the critical exponent of the local susceptibility at the QCP, for example, shows a square-root dependence on $(1/2 - r)$ close to $r = 1/2$; see [19].

In both limits, $r \to 0$ and $r \to 1/2$, we observe that degeneracies due to the combination of single-particle levels, present at the LM and SC fixed points, are lifted at the quantum critical fixed points as soon as one is moving away from $r = 0$ and $r = 1/2$, respectively. This already suggests that the quantum critical point is interacting and cannot be constructed from non-interacting single-particle states.

In the remainder of the paper we want to show how to connect this information from NRG to the perturbative RG of section 3. We know that the critical fixed point can be accessed via two different epsilon-expansions [6, 13] near the two critical dimensions, and, combined with renormalized perturbation theory, these expansions can be used to evaluate various observables near criticality. Here, we will employ this concept to perform renormalized perturbation theory for the entire many-body spectrum at the critical fixed point. To do so, we will start from the many-body spectrum of one of the trivial fixed points, i.e., LM near $r = 0$ and SC near $r = 1/2$, and evaluate corrections to it in lowest-order perturbation theory. This will be done within the NRG concept working directly with the discrete many-body spectra corresponding to a finite NRG chain (which is diagonalized numerically). As the relevant energy scale of the spectra decreases as $\Lambda^{-n/2}$ along the NRG iteration, the strength of the perturbation has to be scaled as well, as the goal is to capture a *fixed point* of the NRG method. This scaling of the perturbation follows precisely from its scaling dimension—the perturbation is marginal at the value of r corresponding to the critical dimension. With the proper scaling, the operator which we use to capture the difference between the free-fermion and critical fixed points becomes exactly marginal (see equations (21) and (37) below).

5.1. Perturbation theory close to $r = 0$

Let us now describe in detail the analysis of the deviation of the QCP levels from the LM levels close to $r = 0$ (the case $r = 1/2$ is discussed in section 5.2). An effective description of the LM fixed point is given by a finite chain with the impurity decoupled from the conduction electron part; see figure 5.

The conduction electron part of the effective Hamiltonian is given by

$$H_{\mathrm{c},N} = \sum_{\sigma n=0}^{N-1} t_n \left(c^\dagger_{n\sigma} c_{n+1\sigma} + c^\dagger_{n+1\sigma} c_{n\sigma} \right). \tag{17}$$

As usual, the structure of the fixed-point spectra depends on whether the total number of sites is even or odd. To simplify the discussion in the following, we only consider a total *odd* number of sites (the flow diagrams of figure 2 are all calculated for this case). For the LM fixed point,

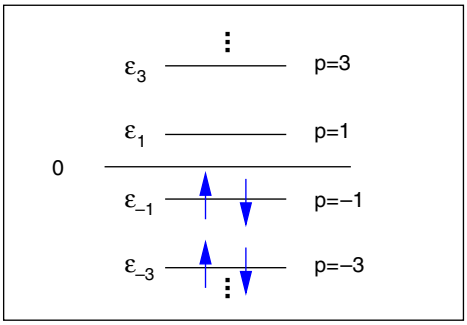

Figure 6. Single-particle spectrum of the free conduction electron chain equation (18). The ground state is given by all the levels with $p < 0$ filled.

this means that the number of sites, $N+1$, of the free conduction electron chain is even, so N in equation (17) is odd.

The single-particle spectrum of the free chain with an even number of sites, corresponding to the diagonalized Hamiltonian

$$\bar{H}_{\mathrm{c},N} = \sum_{\sigma p} \epsilon_p \, \xi^{\dagger}_{p\sigma} \xi_{p\sigma}\,, \tag{18}$$

is sketched in figure 6. (Note that the ϵ_p have to be evaluated numerically.)

As we assume p–h symmetry, the positions of the single-particle levels are symmetric with respect to 0 with

$$\epsilon_p = -\epsilon_{-p}, \qquad p = 1, 3, \ldots, N, \tag{19}$$

and

$$\sum_{p} \equiv \sum_{p=-N,\ p\ \mathrm{odd}}^{p=N} . \tag{20}$$

Note that an equally spaced spectrum of single-particle levels is only recovered in the limit $\Lambda \to 1$ (see figure 6 in [17]) for the case $r = 0$.

The RG analysis of section 3 tells us that the critical fixed point is perturbative accessible from the LM one using a Kondo-type coupling as perturbation. We thus focus on the operator

$$H'_N = \alpha(r)\, f(N)\, \vec{S}_{\mathrm{imp}} \cdot \vec{s}_0, \tag{21}$$

with the goal to calculate the many-body spectrum of the critical fixed point via perturbation theory in H'_N for small r. The function $\alpha(r)$ contains the fixed-point value of the Kondo-type coupling, and $f(N)$ will be chosen such that H'_N is exactly marginal, i.e., the effect of H'_N on the many-particle energies decreases as $\Lambda^{-N/2}$, which is the same N dependence which governs the scaling of the many-particle spectrum itself. The scaling analysis of section 3, equations (3) and (5), suggests a parameterization of the coupling as

$$\alpha(r) = \frac{\mu^{-r}}{\rho_0}\, \alpha\, r, \tag{22}$$

where ρ_0 is the prefactor in the density of states, and μ is a scale of order of the bandwidth—such a factor is required here to make α a *dimensionless* parameter. Thus, the strength of the perturbation increases linearly with r at small r (where $\mu^{-r}/\rho_0 = D + \mathcal{O}(r)$ for a featureless $|\omega|^r$ density of states).

The qualitative influence of the operator $\vec{S}_{\mathrm{imp}} \cdot \vec{s}_0$ on the many-particle states has been discussed in general in [19] for finite r and in [16, 23] for $r = 0$. Whereas an antiferromagnetic exchange coupling is marginally relevant in the gapless case ($r = 0$), it turns out to be irrelevant

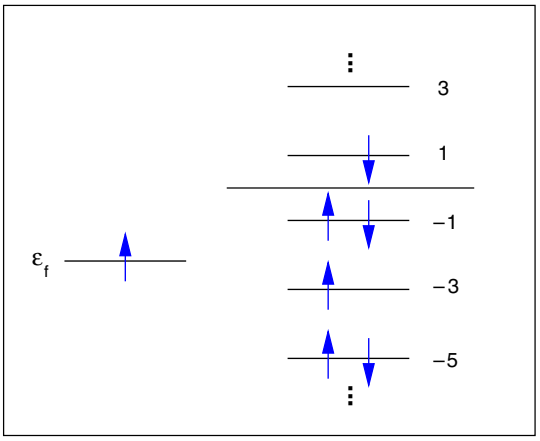

Figure 7. One possible excitation with energy $\epsilon_1 + \epsilon_3$ and quantum numbers $Q = 0$ and $S_z = +1/2$.

for finite r; see [19]. This is of course consistent with the scaling analysis of section 3: the operator (21) simply represents a Kondo coupling, with a tree-level scaling dimension of $\dim[J] = -r$. A detailed analysis of the N-dependence of the operator $\vec{S}_{\rm imp} \cdot \vec{s}_0$ shows that it decreases as $\Lambda^{-Nr/2}\Lambda^{-N/2} = \Lambda^{-N(r+1)/2}$ with increasing N. Consequently, we have to choose

$$f(N) = \Lambda^{Nr/2}. \tag{23}$$

This result also directly follows from $\dim[J] = -r$: as the NRG discretization yields a decrease of the running energy scale of $\Lambda^{-N/2}$, the $\vec{S}_{\rm imp} \cdot \vec{s}_0$ term in H'_N (21) scales as $\Lambda^{-Nr/2}$. The function $f(N)$ is now simply chosen to compensate this effect; using equation (23) the operator H'_N becomes exactly marginal.

Now we turn to a discussion of the many-body spectrum. The relevant ground state of the effective model for the LM fixed point consists of the filled impurity level (with one electron with either spin $\uparrow$ or $\downarrow$) and all the conduction electron states with $p < 0$ filled with both $\uparrow$ and $\downarrow$, as shown in figure 6. Let us now focus on excitations with energy $\epsilon_1 + \epsilon_3$ measured with respect to the ground state. Figure 7 shows one such excitation; in this case, one electron with spin $\downarrow$ is removed from the $p = -3$ level and one electron with spin $\downarrow$ is added to the $p = 1$ level. The impurity level is assumed to be filled with an electron with spin $\uparrow$, so the resulting state has $Q = 0$ and $S_z = +1/2$. In total, there are 32 states with excitation energy $\epsilon_1 + \epsilon_3$. These states can be classified using the quantum numbers Q, S, and S_z.

Here we consider only the states with quantum numbers $Q = 0$, $S = 1/2$, and $S_z = 1/2$ (with excitation energy $\epsilon_1 + \epsilon_3$) which form a four-dimensional subspace. As the state shown in figure 7 is not an eigenstate of the total spin S, we have to form proper linear combinations to obtain a basis for this subspace; this basis can be written in the form

$$\begin{aligned}
|\psi_1\rangle &= \frac{1}{\sqrt{2}} f^\dagger_\uparrow \left(\xi^\dagger_{1\uparrow}\xi_{-3\uparrow} + \xi^\dagger_{1\downarrow}\xi_{-3\downarrow}\right)|\psi_0\rangle \\
|\psi_2\rangle &= \left[\frac{1}{\sqrt{6}} f^\dagger_\uparrow \left(\xi^\dagger_{1\uparrow}\xi_{-3\uparrow} - \xi^\dagger_{1\downarrow}\xi_{-3\downarrow}\right) + \frac{2}{\sqrt{6}} f^\dagger_\downarrow \xi^\dagger_{1\uparrow}\xi_{-3\downarrow}\right]|\psi_0\rangle \\
|\psi_3\rangle &= \frac{1}{\sqrt{2}} f^\dagger_\uparrow \left(\xi^\dagger_{3\uparrow}\xi_{-1\uparrow} + \xi^\dagger_{3\downarrow}\xi_{-1\downarrow}\right)|\psi_0\rangle \\
|\psi_4\rangle &= \left[\frac{1}{\sqrt{6}} f^\dagger_\uparrow \left(\xi^\dagger_{3\uparrow}\xi_{-1\uparrow} - \xi^\dagger_{3\downarrow}\xi_{-1\downarrow}\right) + \frac{2}{\sqrt{6}} f^\dagger_\downarrow \xi^\dagger_{3\uparrow}\xi_{-1\downarrow}\right]|\psi_0\rangle
\end{aligned} \tag{24}$$

where the state $|\psi_0\rangle$ is given by the product of the ground state of the conduction electron chain and the empty impurity level:

$$|\psi_0\rangle = \left[\prod_{p<0} \xi^\dagger_{p\uparrow}\xi^\dagger_{p\downarrow}|0\rangle_{\rm cond}\right] \otimes |0\rangle_{\rm imp}. \tag{25}$$

The fourfold degeneracy of the subspace ($Q = 0$, $S = 1/2$, $S_z = 1/2$) of the LM fixed point at energy $\epsilon_1 + \epsilon_3$ is partially split for finite r in the spectrum of the quantum critical fixed point. Let us now calculate the influence of the perturbation H'_N on the states $|\psi_1\rangle, \ldots, |\psi_4\rangle$, concentrating on the splitting of the energy levels up to first order. Degenerate perturbation theory requires the calculation of the matrix

$$W_{ij} = \langle\psi_i|H'_N|\psi_j\rangle, \qquad i, j = 1, \ldots, 4, \tag{26}$$

and a subsequent calculation of the eigenvalues of $\{W_{ij}\}$ gives the level splitting.

Details of the calculation of the matrix elements W_{ij} are given in appendix A. The result is

$$\{W_{ij}\} = \alpha(r) f(N) \begin{bmatrix} 0 & \frac{\sqrt{3}}{4}\gamma & 0 & 0 \\ \frac{\sqrt{3}}{4}\gamma & -\frac{1}{2}\beta & 0 & 0 \\ 0 & 0 & 0 & \frac{\sqrt{3}}{4}\gamma \\ 0 & 0 & \frac{\sqrt{3}}{4}\gamma & -\frac{1}{2}\beta \end{bmatrix}, \tag{27}$$

with $\gamma = \left[|\alpha_{01}|^2 - |\alpha_{0-3}|^2\right]$ and $\beta = \left[|\alpha_{01}|^2 + |\alpha_{0-3}|^2\right]$. The N-dependence of the coefficients α_{0p} (which relate the operators $c_{0\sigma}$ and $\xi_{p\sigma}$, see equation (A.8)), is given by

$$|\alpha_{0p}|^2 \propto \Lambda^{-Nr/2}\Lambda^{-N/2}, \tag{28}$$

(see also section III A in [19]). Numerically we find that

$$\begin{aligned} \gamma &= -0.1478 \cdot \Lambda^{-Nr/2}\Lambda^{-N/2} \\ \beta &= 2.0249 \cdot \Lambda^{-Nr/2}\Lambda^{-N/2}, \end{aligned} \tag{29}$$

where the prefactors depend on the exponent r and the discretization parameter Λ (the quoted values are for $r = 0.01$ and $\Lambda = 2.0$). The matrix $\{W_{ij}\}_{r=0.01}$ then takes the form

$$\{W_{ij}\}_{r=0.01} = \alpha(r = 0.01)\, \Lambda^{-N/2} \begin{bmatrix} 0 & -0.064 & 0 & 0 \\ -0.064 & -1.013 & 0 & 0 \\ 0 & 0 & 0 & -0.064 \\ 0 & 0 & -0.064 & -1.013 \end{bmatrix}. \tag{30}$$

Diagonalization of this matrix gives the first-order corrections to the energy levels

$$\begin{aligned} \Delta E_1(r = 0.01) &= \Delta E_3(r = 0.01) = \alpha(r = 0.01)\, \Lambda^{-N/2} \cdot (-1.0615) \\ \Delta E_2(r = 0.01) &= \Delta E_4(r = 0.01) = \alpha(r = 0.01)\, \Lambda^{-N/2} \cdot 0.0004 \end{aligned} \tag{31}$$

with

$$E_{N,\rm QCP}(r = 0.01, i) = E_{N,\rm LM}(r = 0.01, i) + \Delta E_i(r = 0.01), \tag{32}$$

($i = 1, \ldots, 4$). Apparently, the fourfold degeneracy of the subspace ($Q = 0$, $S = 1/2$, $S_z = 1/2$) with energy $\epsilon_1 + \epsilon_3$ is split in two levels which are both twofold degenerate.

We repeated this analysis for a couple of other subspaces, and a list of the resulting matrices $\{W_{ij}\}$ and the energy shifts ΔE is given in appendix A.

Let us now proceed with the comparison of the perturbative results with the structure of the quantum critical fixed point calculated from the NRG. For our specific choice of the conduction band density of states, the relation (22) yields $\alpha(r) = \alpha\, r\, D$ for small r (where $\mu^r \approx 1$). Using the corresponding equations for the energy shifts in appendix A, we observe that a *single*

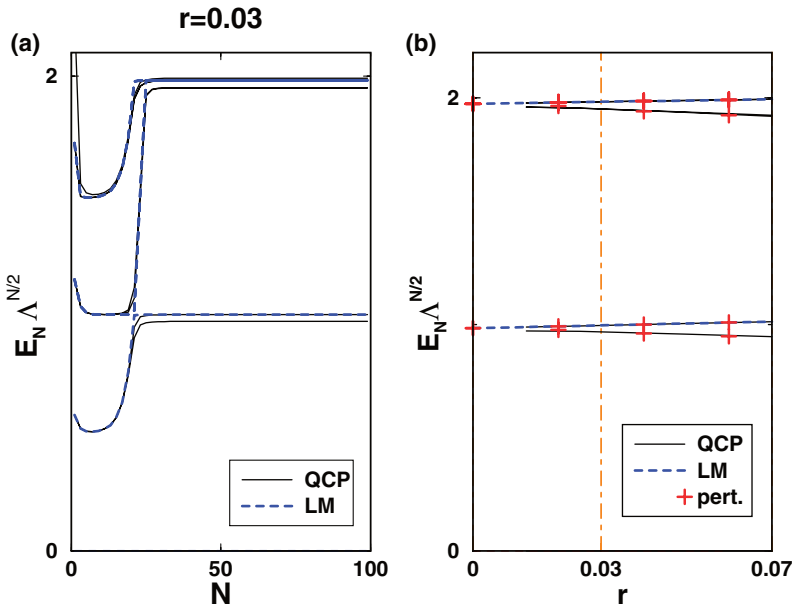

Figure 8. (a) Flow diagram of the lowest-lying energy levels for $r = 0.03$; dashed lines: flow to the LM fixed point; solid lines: flow to the quantum critical fixed point. (b) The deviation of the QCP levels from the LM levels increases linearly with r. This deviation together with the splitting of the energy levels can be explained by the perturbative calculation (crosses) as described in the text.

parameter α must be sufficient to describe the level shifts in *all* subspaces, provided that the exponent r is small enough so that the perturbative calculations are still valid. A numerical fit gives $\alpha \approx 1.03$ for $\Lambda = 2.0$, (the Λ-dependence of α is discussed later; see figure 9).

Figure 8 summarizes the NRG results together with the perturbative analysis for exponents r close to 0. A flow diagram of the lowest-lying energy levels is shown in figure 8(a) for a small value of the exponent, $r = 0.03$, so that the levels of the QCP only slightly deviate from those of the LM fixed point. As discussed above, the deviation of the QCP levels from the LM levels increases linearly with r; see figure 8(b). We indeed get a very good agreement between the perturbative result (crosses) and the NRG data (lines) for exponents up to $r \approx 0.07$. The data shown here are for the subspaces ($Q = 0$, $S = 1/2$, $S_z = 1/2$) and energy $2\epsilon_1$ (the levels at $E_N\Lambda^{N/2} \approx 1$; see appendix A.1) and ($Q = 0$, $S = 1/2$, $S_z = 1/2$) and energy $\epsilon_1 + \epsilon_3$ (the levels at $E_N\Lambda^{N/2} \approx 2$; see the example discussed in this section).

In the NRG, the continuum limit corresponds to the limit $\Lambda \to 1$, but due to the drastically increasing numerical effort upon reducing Λ, results for the continuum limit have to be obtained via extrapolation of NRG data for Λ in, for example, the range $1.5 < \Lambda < 3.0$. Figure 9 shows the numerical results from the NRG calculation together with a linear fit to the data: $\alpha(\Lambda) = 0.985 + 0.045(\Lambda - 1.0)$. Taking into account the increasing error bars for smaller values of Λ, the extrapolated value $\alpha(\Lambda \to 1) \approx 0.985$ is in excellent agreement with the result from the perturbative RG calculation, which is directly for the continuum limit and gives $\alpha = 1.0$.

5.2. *Perturbation theory close to* $r = 1/2$

To describe the deviation of the QCP levels from the SC levels close to $r = 1/2$, we have to start from an effective description of the SC fixed point. This is given by a finite chain *including*

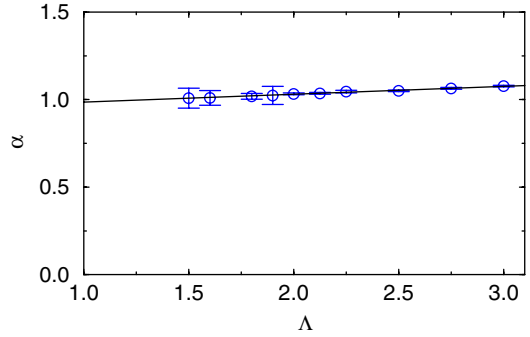

Figure 9. Dependence of the coupling parameter α on the NRG-discretization parameter Λ. The circles correspond to the NRG data and the solid line is a linear fit to the data: $\alpha(\Lambda) = 0.985 + 0.045(\Lambda - 1.0)$.

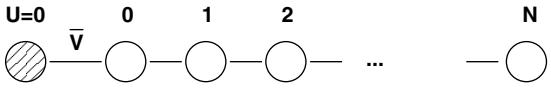

Figure 10. The spectrum of the SC fixed point is described by the non-interacting impurity coupled to the free conduction electron chain.

the impurity site with the Coulomb repulsion $U = 0$ at the impurity site and a hybridization $\bar{V}$ between the impurity and the first conduction electron site; see figure 10.

Note that the SC fixed point can also be described by the limit $\bar{V} \to \infty$ and finite U which means that the impurity and first conduction electron site are effectively removed from the chain. This reduces the number of sites of the chain by two and leads to exactly the same level structure as including the impurity with $U = 0$. However, the description with the impurity included (and $U = 0$) is more suitable for the following analysis.

The corresponding effective Hamiltonian is that of a soft-gap Anderson model on a finite chain with $N + 2$ sites and $\varepsilon_f = U = 0$ (i.e., a p–h symmetric resonant level model).

$$H_{\mathrm{sc},N} = \bar{V} \sum_{\sigma} \left[f_\sigma^\dagger c_{0\sigma} + c_{0\sigma}^\dagger f_\sigma \right] + H_{\mathrm{c},N}, \tag{33}$$

with $H_{\mathrm{c},N}$ as in equation (17).

As for the effective description of the LM fixed point, the effective Hamiltonian is that of a free chain. Focusing, as above, on odd values of N, the total number of sites of this chain, $N + 2$, is odd. The single-particle spectrum of the free chain with an odd number of sites, corresponding to the diagonalized Hamiltonian

$$\bar{H}_{\mathrm{sc},N} = \sum_{\sigma l} \epsilon_l \, \xi_{l\sigma}^\dagger \xi_{l\sigma}, \tag{34}$$

is sketched in figure 11. As we assume p–h symmetry, the positions of the single-particle levels are symmetric with respect to 0 with

$$\epsilon_0 = 0, \qquad \epsilon_l = -\epsilon_{-l}, \qquad l = 2, 4, \ldots, (N + 1), \tag{35}$$

and

$$\sum_l \equiv \sum_{l=-(N+1),\ l \text{ even}}^{l=N+1}. \tag{36}$$

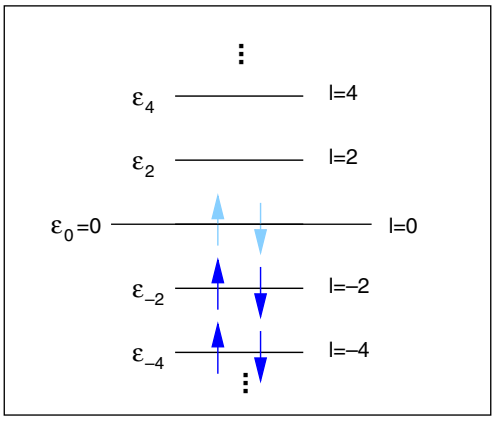

Figure 11. Single-particle spectrum of the free conduction electron chain equation (34). The ground state is fourfold degenerate with all the levels with $l < 0$ filled and the level $l = 0$ either empty, singly ($\uparrow$ or $\downarrow$) or doubly occupied.

The ground state of the effective model for the SC fixed point is fourfold degenerate, with all levels with $l < 0$ filled and the level $l = 0$ either empty, singly ($\uparrow$ or $\downarrow$) or doubly occupied.

According to section 3 the proper perturbation to access the critical fixed point from the SC one is an on-site repulsion, thus we choose

$$H'_N = \beta(r)\bar{f}(N)\,\left(n_{f\uparrow} - \tfrac{1}{2}\right)\left(n_{f\downarrow} - \tfrac{1}{2}\right), \tag{37}$$

($n_{f\sigma} = f^\dagger_\sigma f_\sigma$) with the strength of the perturbation parameterized as

$$\beta(r) = \mu^{2r-1}\rho_0^2\,\bar{V}^4\,\beta\sqrt{1/2 - r}; \tag{38}$$

see section 3. Note that $\rho_0^2(r = 1/2) = 9/(2D^3)$ for a featureless power-law density of states with bandwidth D. The N dependence of the operator $\left(n_{f\uparrow} - \frac{1}{2}\right)\left(n_{f\downarrow} - \frac{1}{2}\right)$ is given by $\Lambda^{(r-1/2)N}\Lambda^{-N/2} = \Lambda^{(r-1)N}$, so we have to choose

$$\bar{f}(N) = \Lambda^{(1/2-r)N}. \tag{39}$$

This again follows from the scaling analysis of section 3: the on-site repulsion has scaling dimension $\dim[U] = 2r - 1$. Thus the $\left(n_{f\uparrow} - \frac{1}{2}\right)\left(n_{f\downarrow} - \frac{1}{2}\right)$ term in H'_N (37) scales as $\Lambda^{N(r-1/2)}$, and $\bar{f}(N)$ (39) compensates this behaviour to make H'_N exactly marginal.

We continue with analysing the low-lying many-body levels. Similarly as above, we focus on one specific example: these are excitations with energy $2\varepsilon_2$ measured with respect to the ground state and quantum numbers $Q = -1$, $S = 0$, and $S_z = 0$. This subspace is two-dimensional and the basis is given by

$$\begin{aligned} |\psi_1\rangle &= -\xi^\dagger_{0\uparrow}\xi^\dagger_{0\downarrow}\xi_{-2\uparrow}\xi_{-2\downarrow}|\psi_0\rangle, \\ |\psi_2\rangle &= \frac{1}{\sqrt{2}}\left(\xi^\dagger_{2\uparrow}\xi_{-2\uparrow} + \xi^\dagger_{2\downarrow}\xi_{-2\downarrow}\right)|\psi_0\rangle, \end{aligned} \tag{40}$$

with

$$|\psi_0\rangle = \prod_{l<0}\xi^\dagger_{l\uparrow}\xi^\dagger_{l\downarrow}|0\rangle. \tag{41}$$

(Note that in this definition of $|\psi_0\rangle$, the $l = 0$ level is empty.)

The twofold degeneracy of this subspace is lifted for $r < 1/2$ in the spectrum of the quantum critical points. The matrix $W_{ij} = \langle\psi_i|H'_N|\psi_j\rangle$ $(i, j = 1, 2)$ is given by

$$\{W_{ij}\} = \beta(r)\bar{f}(N)|\alpha_{f2}|^4 \begin{bmatrix} 2 - 2\kappa + \kappa^2 & 2\sqrt{2}\kappa \\ 2\sqrt{2}\kappa & 2 + \kappa^2 \end{bmatrix}, \tag{42}$$

with $\kappa = |\alpha_{f0}|^2/|\alpha_{f2}|^2$. The N-dependence of the coefficients $|\alpha_{fl}|$ (which relate the operators f_μ and $\xi_{l\mu}$; see equation (B.4)) is given by

$$|\alpha_{fl}|^2 \propto \Lambda^{(r-1)N/2}. \tag{43}$$

Numerically, we find that

$$\begin{aligned} |\alpha_{f2}|^2 &= 0.0366 \cdot (D/\bar{V})^2 \Lambda^{(r-1)N/2} \\ |\alpha_{f0}|^2 &= 0.0930 \cdot (D/\bar{V})^2 \Lambda^{(r-1)N/2}, \end{aligned} \tag{44}$$

where the prefactors depend on the exponent r and the quoted value is for $r = 0.499$. The matrix $\{W_{ij}\}_{r=0.499}$ then takes the form

$$\{W_{ij}\}_{r=0.499} = \beta(r = 0.499)(D/\bar{V})^4 \Lambda^{-N/2} \begin{bmatrix} 0.0044 & 0.0094 \\ 0.0094 & 0.011 \end{bmatrix}. \tag{45}$$

Diagonalization of this matrix gives the first-order corrections to the energy levels

$$\begin{aligned} \Delta E_1(r = 0.499) &= \beta(r = 0.499)(D/\bar{V})^4\, \Lambda^{-N/2} \cdot (-0.0023) \\ \Delta E_2(r = 0.499) &= \beta(r = 0.499)(D/\bar{V})^4\, \Lambda^{-N/2} \cdot (0.018) \end{aligned} \tag{46}$$

with

$$E_{N,\mathrm{QCP}}(r = 0.499, i) = E_{N,\mathrm{SC}}(r = 0.499, i) + \Delta E_i(r = 0.499), \tag{47}$$

$(i = 1, 2)$. We repeated this analysis for a couple of other subspaces, and a list of the resulting matrices $\{W_{ij}\}$ and the energy shifts ΔE is given in appendix B.

The comparison of the perturbative results with the numerical results from the NRG calculation is shown in figure 12(b). As for the case $r \approx 0$, we observe that a single parameter β is sufficient to describe the level shifts in all subspaces, provided the exponent r is close enough to $r = 1/2$ so that the perturbative calculations are valid. For $\Lambda = 2.0$ we find $\beta \approx 70$ and the $\Lambda \to 1$ extrapolation results in $\beta(\Lambda \to 1) \approx 73.0 \pm 5.0$ (the error bars here are significantly larger than those for the extrapolation of the coupling α). The results from perturbative RG, section 3, specifically equations (8) and (10), yield $\beta(r) = \mu^{2r-1}\rho_0^2 \bar{V}^4\, 2\pi^2 u^*$. This gives $\beta = 83.3$.

Similarly to figure 8 above, we show in figure 12(a) a flow diagram for an exponent very close to $1/2$, $r = 0.4985$, so that the levels of the QCP only slightly deviate from those of the SC levels. As discussed above, this deviation is proportional to $\sqrt{1/2 - r}$; see figure 12(b). The data shown here are all for subspaces with $(Q = -1, S = 0, S_z = 0)$; the unperturbed energies E of these subspaces are:

- $E = 0$: the levels at $E_N \Lambda^{N/2} \approx 0$; see appendix B.2,
- $E = \epsilon_2$: the levels at $E_N \Lambda^{N/2} \approx 0.8$; see appendix B.3,
- $E = 2\epsilon_2$: the levels at $E_N \Lambda^{N/2} \approx 1.6$; see the example discussed in this section,
- $E = \epsilon_4$: the levels at $E_N \Lambda^{N/2} \approx 1.8$; see appendix B.4,
- $E = 3\epsilon_2$: the levels at $E_N \Lambda^{N/2} \approx 2.4$.

We again find a very good agreement between the perturbative results (crosses) and the NRG data (lines).

Thus we can summarize that our renormalized perturbation theory for the NRG many-body spectrum works well in the vicinity of both $r = 0$ and $r = 1/2$. In principle, from the many-body spectrum (and suitable matrix elements) all other observables like thermodynamic data

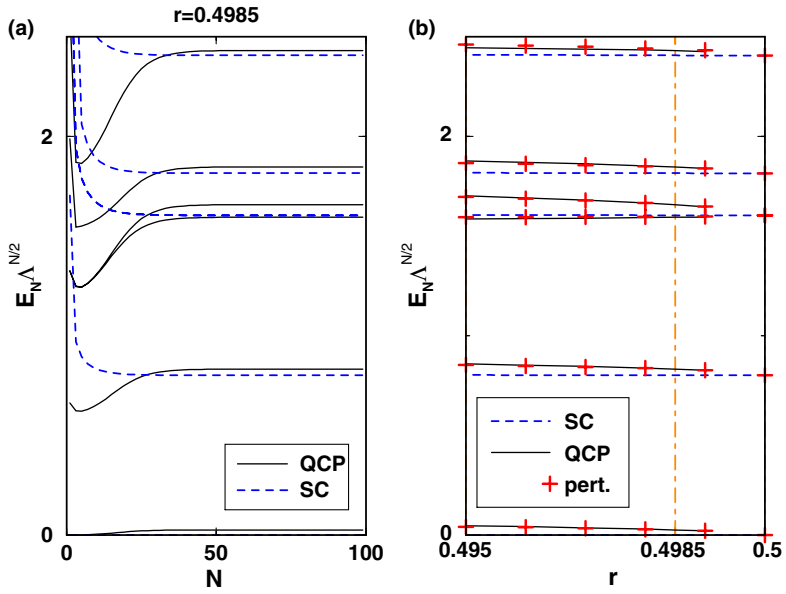

Figure 12. (a) Flow diagram of the lowest-lying energy levels for $r = 0.4985$; dashed lines: flow to the SC fixed point; solid lines: flow to the quantum critical fixed point. (b) The deviation of the QCP levels from the SC levels is proportional to $\sqrt{1/2 - r}$. This deviation together with the splitting of the energy levels can be explained by the perturbative calculation (crosses) as described in the text.

and dynamic correlation functions can be calculated. We note that the convergence radius of the epsilon-expansion for the levels seems to be smaller than that of the direct epsilon-expansion for certain observables like critical exponents and impurity susceptibility and entropy, see [13].

6. Conclusions

Using the quantum phase transitions in the soft-gap Anderson model as an example, we have demonstrated that epsilon-expansion techniques can be used to determine complete many-body spectra at quantum critical points. To this end, we have connected knowledge from standard perturbative RG, which yields information on critical dimensions and parametrically small couplings, and from NRG for the many-body spectra of free-fermion fixed points. Together, these can be used to perform renormalized perturbation theory for many-body spectra of *interacting* intermediate-coupling fixed points. For the soft-gap Anderson model, which features two lower-critical dimensions at $r = 0$ and $r = 1/2$, correspondingly two different approaches can be utilized to capture the same critical fixed point: near $r = 0$ a Kondo term has to be added to a free-fermion chain with a decoupled impurity, whereas near $r = 1/2$ an on-site repulsion is used as a perturbation to the non-interacting Anderson (or resonant-level) model. These perturbations lift the large degeneracies present in the non-interacting spectra, and accurately reproduce the critical spectra determined in NRG calculations at criticality.

Conversely, our method will be useful in situations where the effective low-energy theory for the critical point is not known: a careful analysis of the many-body spectrum near critical dimensions yields information about the scaling dimension and structure of the relevant operators.

For instance, a plot similar to figure 3 can be calculated for the spin-boson model, using the numerical renormalization group method as in [5]. Preliminary results (not shown here) indicate that the many-particle levels of the QCP approach the levels of the delocalized (localized) fixed point in the limit $s \to 0$ ($s \to 1$), with s the exponent of the bath spectral function $J(\omega) \propto \omega^s$.

We envision applications of our ideas to more complex impurity models, for example, with two orbitals or two coupled spins, as well as to non-equilibrium situations treated using NRG [24].

Acknowledgments

We thank S Kehrein, Th Pruschke, and A Rosch for discussions and S Florens, L Fritz, M Kirćan, and N Tong for collaborations on related work. This research was supported by the DFG through SFB 484 (HJL, RB) and the Center for Functional Nanostructures Karlsruhe (MV). MV also acknowledges support from the Helmholtz Virtual Quantum Phase Transitions Institute in Karlsruhe.

Appendix A. Details of the perturbative analysis around the local-moment fixed point

In this appendix, we want to give more details for the derivation of the matrix W_{ij} (equation (27)), which determines the splitting of the fourfold degeneracy of the subspace ($Q = 0$, $S = 1/2$, $S_z = 1/2$) of the LM fixed point at energy $\epsilon_1 + \epsilon_3$. We focus on the matrix element W_{12}:

$$W_{12} = \langle\psi_1|H'_N|\psi_2\rangle = \alpha(r)\, f(N)\, \langle\psi_1|\vec{S}_{\rm imp}\cdot\vec{s}_0|\psi_2\rangle. \tag{A.1}$$

The strategy for the calculations can be extended to the other matrix elements and the other subspaces, for which we add the perturbative results at the end of this appendix without derivation. The operator $\vec{S}_{\rm imp}\cdot\vec{s}_0$ is decomposed in four parts:

$$\vec{S}_{\rm imp}\cdot\vec{s}_0 = \tfrac{1}{2}S^+_{\rm imp}c^\dagger_{0\downarrow}c_{0\uparrow} + \tfrac{1}{2}S^-_{\rm imp}c^\dagger_{0\uparrow}c_{0\downarrow} + \tfrac{1}{2}S^z_{\rm imp}\left(c^\dagger_{0\uparrow}c_{0\uparrow} - c^\dagger_{0\downarrow}c_{0\downarrow}\right), \tag{A.2}$$

so that W_{12} can be written as

$$W_{12} = \alpha(r)\, f(N)\, \tfrac{1}{2}\left[\mathrm{I} + \mathrm{II} + \mathrm{III} - \mathrm{IV}\right], \tag{A.3}$$

with

$$\mathrm{I} = \langle\psi_1|S^+_{\rm imp}c^\dagger_{0\downarrow}c_{0\uparrow}|\psi_2\rangle, \tag{A.4}$$

and the other terms accordingly. With the definitions of $|\psi_1\rangle$ and $|\psi_2\rangle$ of equation (24) we have:

$$\mathrm{I} = \frac{1}{\sqrt{2}}\langle\psi_0|\left(\xi^\dagger_{-3\uparrow}\xi_{1\uparrow} + \xi^\dagger_{-3\downarrow}\xi_{1\downarrow}\right) f_\uparrow S^+_{\rm imp}c^\dagger_{0\downarrow}c_{0\uparrow} \times \left[\frac{1}{\sqrt{6}}f^\dagger_\uparrow\left(\xi^\dagger_{1\uparrow}\xi_{-3\uparrow} - \xi^\dagger_{1\downarrow}\xi_{-3\downarrow}\right) + \frac{2}{\sqrt{6}}f^\dagger_\downarrow\xi^\dagger_{1\uparrow}\xi_{-3\downarrow}\right]|\psi_0\rangle. \tag{A.5}$$

With $S^+_{\rm imp} = f^\dagger_\uparrow f_\downarrow$ we immediately see that the terms containing $f_\uparrow S^+_{\rm imp}f^\dagger_\uparrow$ drop out. The remaining impurity operators, $f_\uparrow S^+_{\rm imp}f^\dagger_\downarrow$, give unity when acting on $|\psi_0\rangle$, so one arrives at

$$\mathrm{I} = \frac{1}{\sqrt{3}}\left[\mathrm{Ia} + \mathrm{Ib}\right], \tag{A.6}$$

with

$$\begin{aligned} \mathrm{Ia} &= \langle\psi_0|\xi^\dagger_{-3\uparrow}\xi_{1\uparrow}c^\dagger_{0\downarrow}c_{0\uparrow}\xi^\dagger_{1\uparrow}\xi_{-3\downarrow}|\psi_0\rangle \\ \mathrm{Ib} &= \langle\psi_0|\xi^\dagger_{-3\downarrow}\xi_{1\downarrow}c^\dagger_{0\downarrow}c_{0\uparrow}\xi^\dagger_{1\uparrow}\xi_{-3\downarrow}|\psi_0\rangle. \end{aligned} \tag{A.7}$$

To analyse Ia and Ib, the operators $c^{(\dagger)}_{0\sigma}$ have to be expressed in terms of the operators $\xi^{(\dagger)}_{p\sigma}$:

$$c_{0\sigma} = \sum_{p'} \alpha_{0p'}\xi_{p'\sigma}, \qquad c^\dagger_{0\sigma} = \sum_{p} \alpha^*_{0p}\xi^\dagger_{p\sigma}, \tag{A.8}$$

with the sums over p and p' defined in equation (20). This gives

$$\mathrm{Ia} = \sum_{pp'} \alpha^*_{0p}\alpha_{0p'}\langle\psi_0|\xi^\dagger_{-3\uparrow}\xi_{1\uparrow}\xi^\dagger_{p\downarrow}\xi_{p'\uparrow}\xi^\dagger_{1\uparrow}\xi_{-3\downarrow}|\psi_0\rangle. \tag{A.9}$$

The only non-zero matrix elements of equation (A.9) are for $p = p' = -3$:

$$\mathrm{Ia} = \alpha^*_{0-3}\alpha_{0-3}\langle\psi_0|\xi^\dagger_{-3\uparrow}\xi_{1\uparrow}\xi^\dagger_{-3\downarrow}\xi_{-3\uparrow}\xi^\dagger_{1\uparrow}\xi_{-3\downarrow}|\psi_0\rangle = -|\alpha_{0-3}|^2. \tag{A.10}$$

Similarly, the term Ib gives

$$\mathrm{Ib} = \sum_{pp'} \alpha^*_{0p}\alpha_{0p'}\langle\psi_0|\xi^\dagger_{-3\downarrow}\xi_{1\downarrow}\xi^\dagger_{p\downarrow}\xi_{p'\uparrow}\xi^\dagger_{1\uparrow}\xi_{-3\downarrow}|\psi_0\rangle = |\alpha_{01}|^2, \tag{A.11}$$

so that, in total,

$$\mathrm{I} = \frac{1}{\sqrt{3}}\left[-|\alpha_{0-3}|^2 + |\alpha_{01}|^2\right]. \tag{A.12}$$

The next term $\mathrm{II} = \langle\psi_1|S^-_{\mathrm{imp}}c^\dagger_{0\uparrow}c_{0\downarrow}|\psi_2\rangle$ gives zero due to the combination of impurity operators: $f_\uparrow f^\dagger_\downarrow f_\uparrow \ldots$ with $f_\uparrow$ from $\langle\psi_1|$ and $f^\dagger_\downarrow f_\uparrow = S^-_{\mathrm{imp}}$.

The third term $\mathrm{III} = \langle\psi_1|S^z_{\mathrm{imp}}c^\dagger_{0\uparrow}c_{0\uparrow}|\psi_2\rangle$ gives

$$\mathrm{III} = \frac{1}{\sqrt{12}}\langle\psi_0|\left(\xi^\dagger_{-3\uparrow}\xi_{1\uparrow} + \xi^\dagger_{-3\downarrow}\xi_{1\downarrow}\right) f_\uparrow S^z_{\mathrm{imp}}c^\dagger_{0\uparrow}c_{0\uparrow}f^\dagger_\uparrow\left(\xi^\dagger_{1\uparrow}\xi_{-3\uparrow} - \xi^\dagger_{1\downarrow}\xi_{-3\downarrow}\right)|\psi_0\rangle, \tag{A.13}$$

where the term with $\frac{2}{\sqrt{6}}f^\dagger_\downarrow\xi^\dagger_{1\uparrow}\xi_{-3\downarrow}$ from $|\psi_2\rangle$ has already been dropped. So we are left with four terms:

$$\mathrm{III} = \frac{1}{\sqrt{12}}\left[\mathrm{IIIa} - \mathrm{IIIb} + \mathrm{IIIc} - \mathrm{IIId}\right], \tag{A.14}$$

with

$$\begin{aligned} \mathrm{IIIa} &= \langle\psi_0|\xi^\dagger_{-3\uparrow}\xi_{1\uparrow}f_\uparrow S^z_{\mathrm{imp}}c^\dagger_{0\uparrow}c_{0\uparrow}f^\dagger_\uparrow\xi^\dagger_{1\uparrow}\xi_{-3\uparrow}|\psi_0\rangle, \\ \mathrm{IIIb} &= \langle\psi_0|\xi^\dagger_{-3\uparrow}\xi_{1\uparrow}f_\uparrow S^z_{\mathrm{imp}}c^\dagger_{0\uparrow}c_{0\uparrow}f^\dagger_\uparrow\xi^\dagger_{1\downarrow}\xi_{-3\downarrow}|\psi_0\rangle, \\ \mathrm{IIIc} &= \langle\psi_0|\xi^\dagger_{-3\downarrow}\xi_{1\downarrow}f_\uparrow S^z_{\mathrm{imp}}c^\dagger_{0\uparrow}c_{0\uparrow}f^\dagger_\uparrow\xi^\dagger_{1\uparrow}\xi_{-3\uparrow}|\psi_0\rangle, \\ \mathrm{IIId} &= \langle\psi_0|\xi^\dagger_{-3\downarrow}\xi_{1\downarrow}f_\uparrow S^z_{\mathrm{imp}}c^\dagger_{0\uparrow}c_{0\uparrow}f^\dagger_\uparrow\xi^\dagger_{1\downarrow}\xi_{-3\downarrow}|\psi_0\rangle. \end{aligned} \tag{A.15}$$

Following similar arguments as above, one obtains

$$\mathrm{IIIa} = \tfrac{1}{2}{\sum_p}'|\alpha_{0p}|^2, \tag{A.16}$$

where the p in $\sum'_p$ takes the values

$$p = 1, -1, -5, -7, \ldots, -N,$$

then

$$\mathrm{IIIb} = \mathrm{IIIc} = 0, \tag{A.17}$$

and

$$\mathrm{IIId} = \tfrac{1}{2}{\sum_{p}}'' |\alpha_{0p}|^2, \tag{A.18}$$

where the p in $\sum''_p$ takes the values

$$p = -1, -3, -5, -7, \ldots, -N.$$

This gives for the third term

$$\mathrm{III} = \frac{1}{\sqrt{12}}\left[\mathrm{IIIa} - \mathrm{IIId}\right] = \frac{1}{4\sqrt{3}}\left[{\sum_{p}}' |\alpha_{0p}|^2 - {\sum_{p}}'' |\alpha_{0p}|^2\right] = \frac{1}{4\sqrt{3}}\left[|\alpha_{01}|^2 - |\alpha_{0-3}|^2\right]. \tag{A.19}$$

The calculation of IV proceeds very similarly to III and one obtains

$$\mathrm{III} = -\mathrm{IV}, \tag{A.20}$$

so that we finally arrive at

$$\begin{aligned} W_{12} &= \alpha(r) f(N) \frac{1}{2}\left(|\alpha_{01}|^2 - |\alpha_{0-3}|^2\right)\left[\frac{1}{\sqrt{3}} + 0 + 2\frac{1}{4\sqrt{3}}\right] \\ &= \alpha(r) f(N) \tfrac{1}{4}\sqrt{3}\left(|\alpha_{01}|^2 - |\alpha_{0-3}|^2\right). \end{aligned} \tag{A.21}$$

We performed a similar analysis for a couple of other subspaces. Here we list the results from the perturbative analysis for three more subspaces together with the corresponding basis states.

A.1. $Q = 0$, $S = 1/2$, $S_z = 1/2$, $E = 2\epsilon_1$

This subspace has the same quantum numbers Q, S and S_z as the one discussed above, so the details of the calculation are very similar. The differences originate from the position of particles and holes in the single-particle spectrum of figure 6. This reduces the dimensionality of the subspace from four to two.

The corresponding basis can be written as

$$\begin{aligned} |\psi_1\rangle &= \frac{1}{\sqrt{2}} f^\dagger_\uparrow (\xi^\dagger_{1\uparrow}\xi_{-1\uparrow} + \xi^\dagger_{1\downarrow}\xi_{-1\downarrow})|\psi_0\rangle, \\ |\psi_2\rangle &= \left[\frac{1}{\sqrt{6}} f^\dagger_\uparrow (\xi^\dagger_{1\uparrow}\xi_{-1\uparrow} - \xi^\dagger_{1\downarrow}\xi_{-1\downarrow}) + \frac{2}{\sqrt{6}} f^\dagger_\downarrow \xi^\dagger_{1\uparrow}\xi_{-1\downarrow}\right]|\psi_0\rangle. \end{aligned} \tag{A.22}$$

The first-order corrections are given by the 2×2 matrix

$$\{W_{ij}\} = \alpha(r) f(N) \begin{bmatrix} 0 & \frac{\sqrt{3}}{4}\gamma \\ \frac{\sqrt{3}}{4}\gamma & -\frac{1}{2}\beta \end{bmatrix}, \tag{A.23}$$

with $\gamma = |\alpha_{01}|^2 - |\alpha_{0-1}|^2$ and $\beta = |\alpha_{01}|^2 + |\alpha_{0-1}|^2$. Due to the particle–hole symmetry of the conduction band we have $|\alpha_{01}| = |\alpha_{0-1}|$; therefore, the off-diagonal matrix elements vanish and the effect of the perturbation is simply a negative energy shift only for the state $|\psi_2\rangle$:

$$\{W_{ij}\} = \alpha(r) f(N) \begin{bmatrix} 0 & 0 \\ 0 & -|\alpha_{01}|^2 \end{bmatrix}. \tag{A.24}$$

This effect can be seen in the energy splitting of the first two low-lying excitations in figure 8.

A.2. $Q = -1, S = 0, E = -\epsilon_{-1}$

There is only one configuration for this combination of quantum numbers and excitation energy:

$$|\psi\rangle = \frac{1}{\sqrt{2}}(f_\uparrow^\dagger \xi_{-1\uparrow} + f_\downarrow^\dagger \xi_{-1\downarrow})|\psi_0\rangle. \tag{A.25}$$

The first-order perturbation keeps the state in this one-dimensional subspace and the energy correction is given by

$$\Delta E = \langle\psi|H_N'|\psi\rangle = -\tfrac{3}{4}\alpha(r) f(N)|\alpha_{0-1}|^2. \tag{A.26}$$

A.3. $Q = -1, S = 0, E = -\epsilon_{-3}$

The difference to the previous case is the position of the hole in the single-particle spectrum. The state is now given by

$$|\psi\rangle = \frac{1}{\sqrt{2}}(f_\uparrow^\dagger \xi_{-3\uparrow} + f_\downarrow^\dagger \xi_{-3\downarrow})|\psi_0\rangle, \tag{A.27}$$

with the energy correction

$$\Delta E = \langle\psi|H_N'|\psi\rangle = -\tfrac{3}{4}\alpha(r) f(N)|\alpha_{0-3}|^2. \tag{A.28}$$

Appendix B. Details of the perturbative analysis around the strong coupling fixed point

The main difference in the calculation of the matrix elements $\{W_{ij}\}$ for this case is due to the structure of the perturbation; see equation (37). Furthermore the ground state of the SC fixed point is fourfold degenerate and the perturbation partially splits this degeneracy, as discussed in the following.

B.1. $Q = 0, S = 1/2, S_z = 1/2, E = 0$

This is one of the four degenerate ground states at the SC fixed point:

$$|\psi_1\rangle = \xi_{0\uparrow}^\dagger|\psi_0\rangle, \tag{B.1}$$

with $|\psi_0\rangle$ defined in equation (41).

The perturbative correction is given by

$$\langle\psi_1|H_N'|\psi_1\rangle = \tfrac{1}{2}\beta(r)\bar{f}(N)(1 - |\alpha_{f0}|^4) \tag{B.2}$$

which corresponds to the energy shift of the ground state:

$$\Delta E_1 = \tfrac{1}{2}\beta(r)\bar{f}(N)(1 - |\alpha_{f0}|^4). \tag{B.3}$$

The coefficients α_{fl} are defined via the relation between the operators $f_\sigma^{(\dagger)}$ and $\xi_{l\sigma}^{(\dagger)}$:

$$f_\sigma = \sum_{l'} \alpha_{fl'}\xi_{l'\sigma}, \qquad f_\sigma^\dagger = \sum_l \alpha_{fl}^*\xi_{l\sigma}^\dagger. \tag{B.4}$$

B.2. $Q = -1, S = 0, E = 0$

This state is also a ground state in the $U = 0$ case:

$$|\psi_2\rangle = |\psi_0\rangle. \tag{B.5}$$

The calculation of the first-order correction for $|\psi_2\rangle$ gives

$$\langle\psi_2|H'_N|\psi_2\rangle = \tfrac{1}{2}\beta(r)\bar{f}(N)(1 + |\alpha_{f0}|^4). \tag{B.6}$$

This means that the ground state including the effect of the perturbation is given by $|\psi_1\rangle$ in equation (B.1) and the state $|\psi_2\rangle$ appears as an excited state. For a comparison with the energy levels shown in the NRG flow diagrams, where the ground-state energy is set to zero in each iteration, we subtract the perturbative correction of the ground state (ΔE_1) from the energies of all other excited states. Subtracting this energy shift from equation (B.6) gives the net energy correction for the $|\psi_2\rangle$ state:

$$\Delta E_2 = \beta(r)\bar{f}(N)|\alpha_{f0}|^4. \tag{B.7}$$

B.3. $Q = -1, S = 0, E = \epsilon_2$

The state corresponding to this subspace is given by

$$|\psi_3\rangle = \frac{1}{\sqrt{2}}(\xi^\dagger_{0\uparrow}\xi_{-2\uparrow} + \xi^\dagger_{0\downarrow}\xi_{-2\downarrow})|\psi_0\rangle. \tag{B.8}$$

The first-order correction reads

$$\langle\psi_3|H'_N|\psi_3\rangle = \beta(r)\bar{f}(N)\left[\tfrac{1}{2}(1 - |\alpha_{f0}|^4) + 3|\alpha_{f0}|^2|\alpha_{f-2}|^2\right]. \tag{B.9}$$

Subtracting the energy correction for the ground state results in

$$\Delta E_3 = 3\beta(r)\bar{f}(N)|\alpha_{f0}|^2|\alpha_{f-2}|^2. \tag{B.10}$$

B.4. $Q = -1, S = 0, E = \epsilon_4$

Similarly, for the state

$$|\psi_4\rangle = \frac{1}{\sqrt{2}}(\xi^\dagger_{0\uparrow}\xi_{-4\uparrow} + \xi^\dagger_{0\downarrow}\xi_{-4\downarrow})|\psi_0\rangle, \tag{B.11}$$

the first-order correction is given by

$$\langle\psi_4|H'_N|\psi_4\rangle = \beta(r)\bar{f}(N)\left[\tfrac{1}{2}(1 - |\alpha_{f0}|^4) + 3|\alpha_{f0}|^2|\alpha_{f-4}|^2\right], \tag{B.12}$$

and subtracting the energy correction for the ground state results in

$$\Delta E_4 = 3\beta(r)\bar{f}(N)|\alpha_{f0}|^2|\alpha_{f-4}|^2. \tag{B.13}$$

References

[1] Bulla R and Vojta M 2003 *Concepts in Electron Correlations* ed A C Hewson and V Zlatić (Dordrecht: Kluwer–Academic) p 209
Vojta M 2004 *Preprint* cond-mat/0412208
[2] Vojta M 2003 *Rep. Prog. Phys.* **66** 2069 (section 4)
[3] Affleck I 2005 *J. Phys. Soc. Japan* **74** 59
[4] Leggett A J, Chakravarty S, Dorsey A T, Fisher M P A, Garg A and Zwerger W 1987 *Rev. Mod. Phys.* **59** 1
[5] Bulla R, Tong N and Vojta M 2003 *Phys. Rev. Lett.* **91** 170601
[6] Vojta M and Kirćan M 2003 *Phys. Rev. Lett.* **90** 157203
Kirćan M and Vojta M 2004 *Phys. Rev.* B **69** 174421

[7] De Leo L and Fabrizio M 2005 *Phys. Rev. Lett.* **94** 236401
[8] Craig N J, Taylor J M, Lester E A, Marcus C M, Hanson M P and Gossard A C 2004 *Science* **304** 565
[9] Le Hur K 2004 *Phys. Rev. Lett.* **92** 196804
Li M-R and Le Hur K 2004 *Phys. Rev. Lett.* **93** 176802
[10] Khveshchenko D V 2004 *Phys. Rev.* B **69** 153311
[11] Si Q, Rabello S, Ingersent K and Smith J L 2001 *Nature* **413** 804
Si Q, Rabello S, Ingersent K and Smith J L 2003 *Phys. Rev.* B **68** 115103
[12] Withoff D and Fradkin E 1990 *Phys. Rev. Lett.* **64** 1835
[13] Vojta M and Fritz L 2004 *Phys. Rev.* B **70** 094502
Fritz L and Vojta M 2004 *Phys. Rev.* B **70** 214427
[14] Logan D E and Glossop M T 2000 *J. Phys.: Condens. Matter* **12** 985
[15] Glossop M T and Logan D E 2003 *J. Phys.: Condens. Matter* **15** 7519
[16] Wilson K G 1975 *Rev. Mod. Phys.* **47** 773
[17] Bulla R, Hewson A C and Zhang G-M 1997 *Phys. Rev.* B **56** 11721
[18] Hewson A C 1993 *The Kondo Problem to Heavy Fermions* (Cambridge: Cambridge University Press)
[19] Gonzalez-Buxton C and Ingersent K 1998 *Phys. Rev.* B **57** 14254
[20] Bulla R, Pruschke T and Hewson A C 1997 *J. Phys.: Condens. Matter* **9** 10463
Bulla R, Glossop M T, Logan D E and Pruschke T 2000 *J. Phys.: Condens. Matter* **12** 4899
[21] Vojta M and Bulla R 2002 *Phys. Rev.* B **65** 014511
[22] Chen K and Jayaprakash C 1995 *J. Phys.: Condens. Matter* **7** L491
[23] Krishna-murthy H R, Wilkins J W and Wilson K G 1980 *Phys. Rev.* B **21** 1003
Krishna-murthy H R, Wilkins J W and Wilson K G 1980 *Phys. Rev.* B **21** 1044
[24] Anders F B and Schiller A 2005 *Preprint* cond-mat/0505553